Wireless Power Supply of Moving Linear Actuator Enclosed in Stainless-Steel

Spasoje Mirić[1], Junzhong Xu[1], Jonas Huber[1], Dominik Bortis[1], Marco Hitz[2], Johann W. Kolar[1]

[1] Power Electronic Systems Laboratory, ETH Zurich, Zurich, Switzerland

[2] NTI AG, Spreitenbach, Switzerland

E-mail: miric@lem.ee.ethz.ch

Abstract—Linear actuators are a key element of automatized industrial systems, as linear motion is present in most manipulation tasks. For actuators performing x-z movements, actuator windings are placed on the moving part and these must be supplied. However, in high-purity environments such as in the food processing or pharmaceutical industries, actuators should be fully enclosed in stainless steel (SS) to facilitate thorough cleaning, and cables are undesirable. This paper therefore proposes high-efficiency (97 % at 100 W) wireless power transfer (WPT) through two 0.5 mm thick SS enclosures, which facilitates the deployment of linear actuators in high-purity environments. The proposed coaxial transformer arrangement with the magnetic core mounted on the moving part results in a magnetic field that is in parallel to the SS enclosures, which minimizes eddy-current losses. We discuss the detailed modeling and optimization of the system, and finally present an industrial two-axis actuator prototype that fully confirms the theoretical analysis.

Index Terms—Wireless Power Transfer, WPT, Inductive Power Transfer, IPT, Coaxial WPT, Metal Enclosure, Resonant Compensation, SRC operation.

I. INTRODUCTION

Linear actuators are used in a wide range of different application areas ranging from automotive, e.g., for active suspension of vehicles [1], to industry automatization, e.g., for various handling and manipulation tasks. Such pick-and-place applications include, e.g., moving and placing small components for semiconductor packaging [2]. Similar solutions are also employed in the pharmaceutical industry (e.g., for the dosing of liquids) and in the food processing industry for handling foodstuffs. In such environments, highest hygiene is of paramount importance. Accordingly, all equipment, i.e., also the linear actuators, must ideally be fully enclosed in stainless-steel (SS) housings to facilitate thorough cleaning and/or disinfection.

However, linear pick-and-place actuators with long stroke lengths are usually built as shown in **Fig. 1**, i.e., the slider (with the electrically supplied windings) moves in x-direction along a fixed stator, i.e., an SS rod that contains stacked permanent magnets (PMs). The slider's typical payload is another actuator, e.g., for z-direction movements, and/or end effectors (e.g., manipulation tools) which also need to be supplied with power. Thus, a cable connection (power supply, sensing) to the actuator's moving part is required. These cables are typically
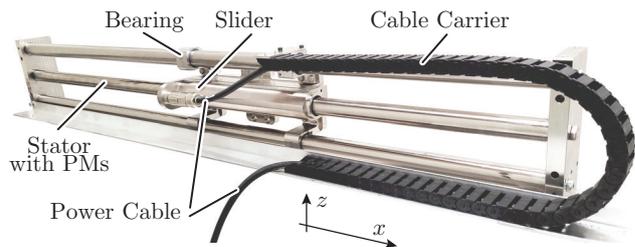
Fig. 1: Stainless-steel-(SS)-enclosed linear actuator with a fixed stator and the slider performing the linear motion. Typically, the slider carries an end effector, e.g. a linear actuator allowing positioning in z-direction. Conventionally, the windings of the slider and the end effector are supplied via cables guided in cable carriers, which cannot be enclosed in SS and are difficult to clean.

guided in flexible cable carriers (cf. **Fig. 1**). Clearly, such cable and cable carrier assemblies cannot be enclosed in SS, and are in general difficult to clean. In addition, such systems have drawbacks like a limited lifetime, since cable carriers wear out and the cables themselves break after a certain number of bending cycles; this wear-and-tear generates small particles that can contaminate the environment. Therefore, there is a need to eliminate the moving cables and cable carriers from linear actuator systems; especially for applications that require complete SS enclosures.

Wireless power transfer (WPT) to the moving part of the linear actuator (cf. **Fig. 1**) could be used to replace the cables and cable carriers. Examples of such linear actuators (in a wide sense, i.e., including wireless power supply of traction units) with WPT have been reported in the literature [3]–[7], and by now WPT is an established solution for various applications. However, all systems reported so far lack the SS enclosures that are needed for applications in high-purity environments as discussed above.

If an SS enclosure between the moving and the stationary parts of a WPT system is present, the magnetic coupling field $\vec{B}$ fundamentally required for (near field) WPT interacts with the electrically conductive SS enclosure and causes eddy-current losses that deteriorate the WPT efficiency. Depending on the WPT coil arrangement, the field passes orthogonally through the SS enclosures (cf. **Fig. 2(a)**). In this orthogonal-field concept (OFC), the area A_{ofc} where eddy currents are induced can be large, causing high losses; [8], [9] have found
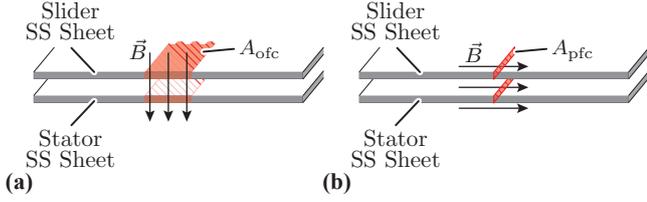
Fig. 2: Types of the WPT through SS: **(a)** Orthogonal-field concept (OFC), where the field lines and the SS sheets are orthogonal and **(b)** parallel-field concept (PFC), where the field lines and the field lines are in parallel.

maximum efficiencies of around $72\,\%$ for WPT through two $0.5\,\text{mm}$ SS sheets. Alternatively, a parallel-field concept (PFC, cf. **Fig. 2(b)**) could be employed, where the field is oriented in parallel to the SS enclosures. Therefore, eddy currents are induced only in a much smaller area A_{pfc} (low induced voltage and high resistance), that is defined by the thickness of the SS sheets.

In this paper, we propose a WPT system for SS-enclosed linear actuators that employs the PFC and hence achieves high efficiencies. Considering an exemplary $72\,\text{V}$ DC (input and output), $\geq 100\,\text{W}$ system, we discuss the detailed magnetic circuit and SS loss modeling in **Section II**, and voltage-impressed operation as a DC transformer in **Section III**. **Section IV** finally presents an industrial actuator prototype that fully confirms the theoretical analysis.

II. MODELING OF THE PARALLEL FIELD CONCEPT WPT

To achieve WPT with a magnetic field that is in parallel to the SS enclosures, a *coaxial* arrangement [3], including a magnetic core on the moving part, as shown in **Fig. 3(a)** can be employed. The primary winding is placed inside an SS tube long enough to cover the linear motion's stroke. This winding creates a tangential flux density $B(r)$ that is in parallel to the wall of the SS tube, resulting in the PFC depicted in **Fig. 2(b)**. Note that the coaxial SS enclosure covering the magnetic core is not shown for better visibility.

A. SS Loss Model

As the field penetrates through the SS tube wall cross section $A_{\text{pfc}} = \delta_{\text{ss}} L_{\text{ss}}$, the calculation of the eddy-current losses is similar as for those in a lamination sheet of a laminated magnetic core, i.e.,

$$P_{\text{ss}} = \frac{V_{\text{ss}}}{24}\sigma_{\text{ss}}\delta_{\text{ss}}^2 \omega_{\text{s}}^2 F(\chi)\hat{B}_{\text{ss}}^2, \tag{1}$$

where $\sigma_{\text{ss}} = 1.3 \times 10^6\,\text{S/m}$ is the conductivity of the SS, $\omega_{\text{s}} = 2\pi f_{\text{s}}$ is the angular frequency, $\hat{B}_{\text{ss}}$ is the average flux density in the SS, δ_{ss} is the SS tube wall thickness, $V_{\text{ss}} = \pi d_{\text{ss}}\delta_{\text{ss}} L_{\text{ss}}$ is the SS volume and $F(\chi)$ models the skin effect in the SS tube (cf. [10]), where $\chi = \delta_{\text{ss}}/\delta_{\text{ss,skin}}$ is the ratio of the SS tube wall thickness δ_{ss} and the skin depth for the SS:

$$\delta_{\text{ss,skin}} = \sqrt{\frac{2}{\sigma_{\text{ss}}\mu_0\,\omega}}. \tag{2}$$

(a)

(b)
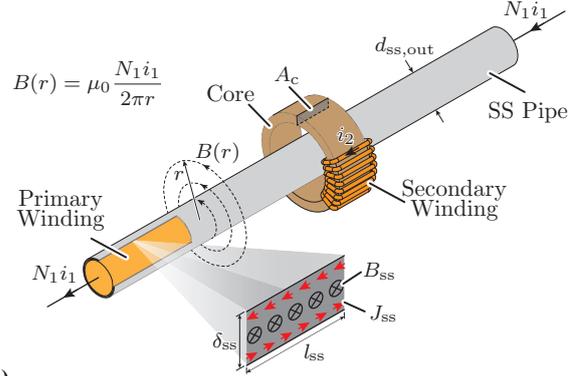
Fig. 3: **(a)** Primary and secondary winding arrangement of the PFC. The primary winding is enclosed in an SS tube with $\delta_{\text{ss}} = 0.5\,\text{mm}$, $d_{\text{ss}} = 20\,\text{mm}$ and a total length of $l_{\text{ss}} = 1180\,\text{mm}$. As conceptually shown in **Fig. 2(b)**, the flux density B_{ss} induces eddy currents J_{ss} only in the relatively small area defined by the SS tube wall thickness and length. **(b)** Normalized skin effect impact $F(\chi)$ onto the SS resistance R_{ss} from (3), where $\chi = \delta_{\text{ss}}/\delta_{\text{ss,skin}}$ is the ratio of the SS tube wall thickness δ_{ss} and the SS skin depth $\delta_{\text{SS,skin}}$, cf. (2). The detailed analytic derivation of F is given in [10].

As the flux density in the SS tube walls decays with $\sim 1/r$, $\hat{B}_{\text{ss}}$ is its average value over the wall thickness calculated as $\hat{B}_{\text{ss}} = 1/\delta_{\text{ss}}\int_{r_{\text{ss,in}}}^{r_{\text{ss,out}}}\hat{B}(r)dr$, where $r_{\text{ss,out}} = d_{\text{ss,out}}/2$, $r_{\text{ss,in}} = r_{\text{ss,out}} - \delta_{\text{ss}}$, $\hat{B}(r) = \mu_0 N_1\hat{I}_1/(2\pi r)$ and, $\hat{I}_1$ is the primary current amplitude, i.e., $i_1 = \hat{I}_1\cos(\omega t)$. Therefore, the SS loss formula (1) can be expressed as a function of the primary current amplitude as

$$P_{\text{ss}} = \frac{1}{2}\cdot\underbrace{\frac{V_{\text{ss}}}{12}\sigma_{\text{ss}}\omega_{\text{s}}^2 F(\chi)\frac{\mu_0^2 N_1^2}{4\pi^2}\ln^2\left(\frac{d_{\text{ss,out}}}{d_{\text{ss,in}}}\right)}_{=R_{\text{ss}}}\cdot\hat{I}_1^2. \tag{3}$$

Thus, the SS losses can be modeled in the same way as (primary-side) winding transformer winding losses, i.e., as a resistor R_{ss} that can be included in the transformer equivalent circuit in series with the primary winding resistance. The skin effect for the calculation of the SS tube resistance is modeled with $F(\chi)$, which is depicted in **Fig. 3(b)**. It clearly shows that for the tube thicknesses lower then the SS skin depth, i.e., for $\delta_{\text{ss}} \leq \delta_{\text{ss,skin}}$, the high-frequency skin effect in the SS tube can be neglected, i.e., $F \approx 1$. For example, the SS skin depth at $100\,\text{kHz}$ is $\delta_{\text{ss,skin}}(100\,\text{kHz}) = 1.4\,\text{mm}$, if $\sigma_{\text{ss}} = 1.3 \times 10^6\,\text{S/m}$ is assumed.

B. Primary Winding Design and Loss Model

The primary winding is enclosed inside an SS tube (see **Fig. 3**). As the winding carries AC currents with high fre-
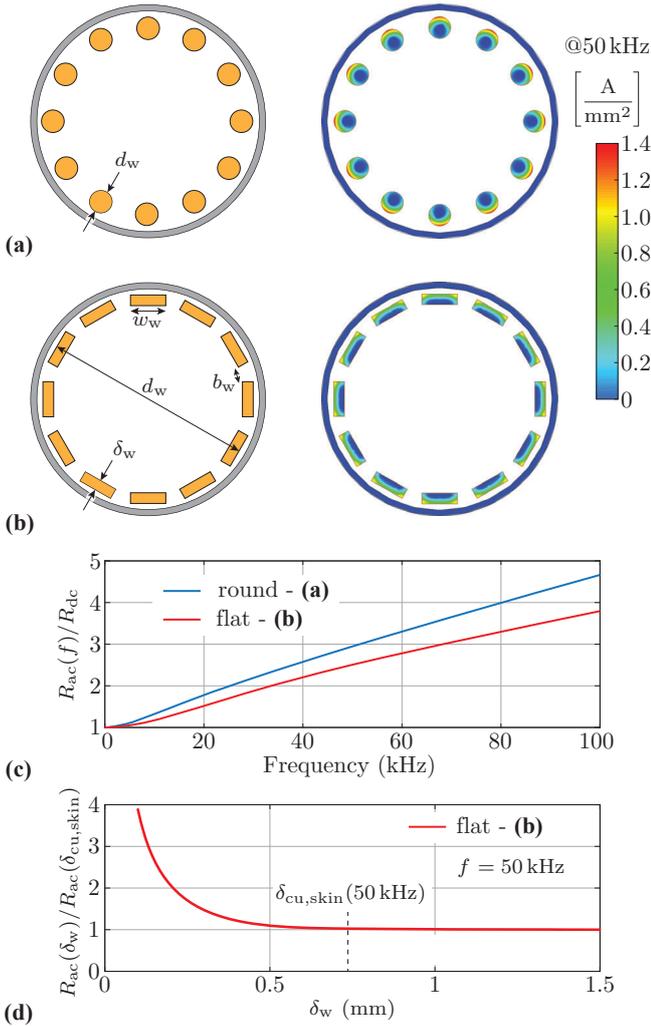
Fig. 4: Primary winding with $N_1 = 12$, built with circular arrangement of the conductors and maximum conductor distance (wires close to the SS tube wall) for reduced AC winding resistance: **(a)** round wire with $d_w = 1.85$ mm and **(b)** flat wire (of equal cross section area) with $\delta_w = 0.9$ mm, $w_w = 3$ mm, $b_w = 1.2$ mm and $d_w = 17$ mm; current distribution on the right hand side for $\hat{I}_1 = 1$ A per wire. **(c)** Ratio of the primary winding's AC and DC resistances for the configurations from **(a)** and **(b)**. **(d)** Normalized winding resistance versus the winding thickness δ_w for $f = 50$ kHz, showing that increasing wire thickness beyond the skin depth does not reduce the winding's AC resistance anymore.

quencies, high-frequency effects that increase the winding resistance must be considered. Note that we consider only solid wires in the design, as it allows simpler/cost-effective manufacturing of the primary winding compared to using litz wire. To find the best possible arrangement of the wires, 2D-FEM analysis is used. The lowest AC resistance results if the wires are placed only at the circumference, close to the SS tube wall, like in **Fig. 4(a)**. The exemplary current distribution at 50 kHz clearly highlights the skin effect in the conductors, i.e., a part of a round wire's cross section is barely carrying current. Therefore, using a flat wire for the primary winding like in
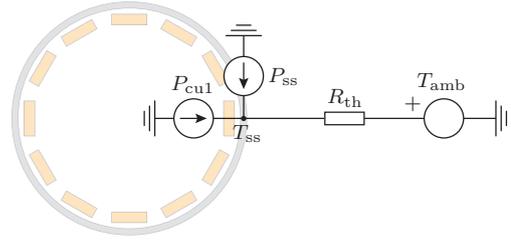
Fig. 5: Primary-side thermal model, where the equivalent thermal resistance between the surface of the tube and the ambient is measured as $R_{th} = 1.5$ W/K (for one meter of the SS tube length, i.e., for $L_{ss} = 1$ m, and $T_{ss} = 60\,°C$, $T_{amb} = 40\,°C$, horizontal orientation and natural convection).

Fig. 4(b) reduces the AC winding resistance as compared to a round wire of equal cross section (cf. **Fig. 4(c)**). Finally, for the desired operating frequency f_s, a reasonable flat wire thickness δ_w that is smaller or equal to the skin depth for the copper $\delta_{cu,skin}$ should be chosen, i.e., $\delta_w \leq \delta_{cu,skin}$. **Fig. 4(d)** depicts the dependence of the flat wire resistance on its thickness δ_w at $f_s = 50$ kHz, which shows that increasing δ_w above the skin depth does not lead to a further reduction of the winding resistance anymore. Therefore, the effectively available copper area A_w depends on the operating frequency f and the winding diameter d_w given by the SS tube as

$$A_w(f) = (d_w \pi - N_1 b_w) \cdot \delta_{cu,skin}(f), \qquad (4)$$

where N_1 is the primary number of turns and b_w is the distance between the individual wires, cf. **Fig. 4(d)**. Consequently, to increase the copper area beyond what is given by $A_w(f)$ in (4), the winding diameter d_w, i.e., SS tube diameter, should be increased. The difference between the inner SS tube diameter $d_{ss,in}$ and the winding diameter d_w depends on the thickness of the required electrical insulation $\delta_{insulation}$; for the considered voltages it is ideally in the sub-millimeter range, i.e., $(d_{ss,in} - d_w)/2 = \delta_{insulation} < 1$ mm.

C. SS Tube Thermal Model

In most applications, the SS surface temperature T_{ss} should be kept below $60\,°C$ to prevent injuries in case of accidental touch by operating personnel. To determine the relation between the primary-side losses and T_{ss}, the thermal model depicted in **Fig. 5** is used, which accounts for the primary winding copper losses P_{cu1} and the SS losses P_{ss} (cf. (1)). The equivalent thermal resistance R_{th} is measured by imposing known P_{ss} losses and keeping $P_{cu1} = 0$, which gives $R_{th} = (T_{ss} - T_{amb})/P_{ss} = 1.5$ K/W, for a 1 m long and 20 mm diameter SS tube; T_{ss} is measured with a thermal camera at $T_{amb} = 40\,°C$. This results in a natural convection heat transfer h_{ss} coefficient for the SS tubes of around $h_{ss} = 1/(R_{th} A_{ss}) \approx 10.6$ W/(Km^2), which is used to predict the maximum possible losses in the primary. For example, to keep $T_{ss} < 60\,°C$ at $T_{amb} = 40\,°C$, the losses in the primary (1 m long, 20 mm diameter SS tube) should be $P_{cu1} + P_{ss} < 13.3$ W.
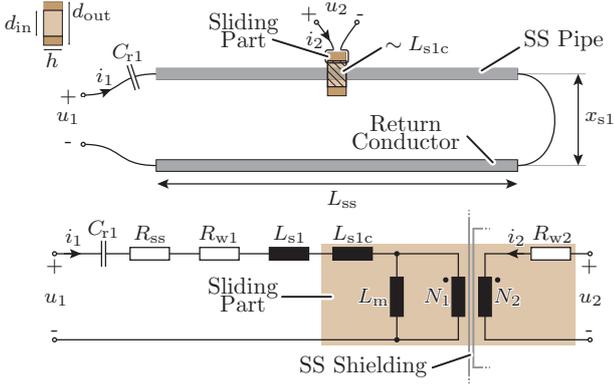
Fig. 6: PFC WPT system with a single receiver: conceptual physical arrangement and electrical equivalent circuit. The resistance R_{w1}, the stray inductance L_{s1} and L_{s1c} model the primary winding. The resistance R_{ss} models the impact of the SS tube enclosure and it is calculated according to (3).

D. Electric Equivalent Circuit

The electric circuit model is shown in **Fig. 6**, together with the conceptual physical arrangement of the system. The resistance R_{w1} depends on the operating frequency, i.e., $R_{s1} = R_{ac}(f)$, and the winding geometry (cf. **Fig. 4(b)**, in the following the flat winding geometry is assumed). The DC component of R_{w1} is calculated analytically and the frequency impact obtained as discussed in **Section II-B** above. Assuming a return conductor that is straight and placed in parallel to the SS tube at a distance of x_{s1} facilitates a straightforward estimation of the external stray inductance as $L_{s1} = \mu_0 \log(x_{s1}/(d_w/2))L_{ss}N_1^2/\pi$. The internal stray inductance from the portion of the primary covered by the secondary core is much smaller than L_{s1} and it can be approximated as $L_{s1c} = L_{s1}(h/L_{ss})$, where h is the secondary core height and L_{ss} is the length of the primary SS tube. The magnetization inductance is calculated from the A_L value of the core as $L_m = A_L N_1^2$. Vitroperm 500F is used as core material, since it performs better at lower frequencies than ferrite [11]; i.e., the higher saturation flux density enables choosing smaller and lighter cores and ultimately lower losses. As shown earlier in **Section II-A**, the SS losses are solely caused by the primary current i_1 and, they can be modeled with a series resistance R_{ss}, like (primary) winding losses. Note that this is different than in OFC WPT (cf. [8]), where the SS losses depend on the air gap field, i.e., finally on the primary and the secondary currents, and thus must be modelled in the equivalent circuit as a resistor in parallel to the magnetizing inductance (like core losses).

III. MODE OF OPERATION AND POWER ELECTRONICS

A. Voltage-Impressed DCX Operation

The use of a magnetic core results in a high magnetic coupling (cf. **Fig. 6**), which allows to operate the WPT system as a series resonant converter whereby the resonant capacitor

(a)

(b) **(c)**

(d)
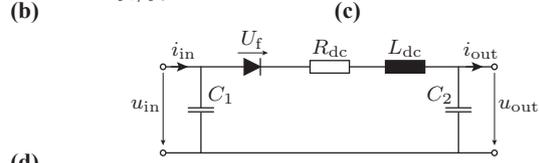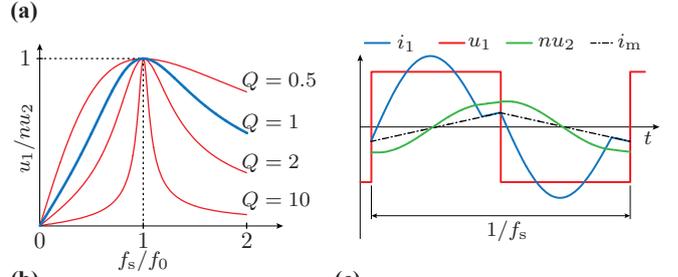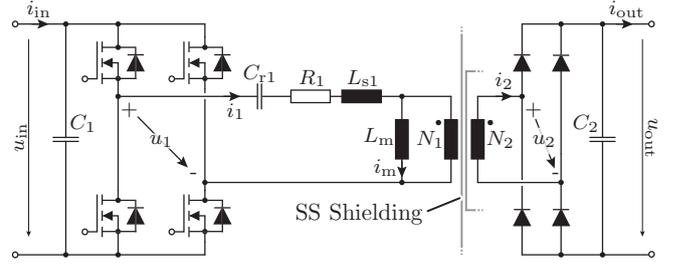
Fig. 7: (a) Operation of the PFC WPT system as a "DC-transformer" (DCX), which is enabled by the high magnetic coupling: resonant compensation of L_{s1} by C_{r1} results in **(b)** load-independent voltage gain for operation at (or slightly below) the resonant frequency, and in **(c)** the typical voltage and current waveforms. **(d)** Dynamic equivalent circuit modeling the terminal behavior [12], [13], i.e., the DCX ensures a tight coupling of the input and output DC voltages without the need for closed-loop control.

C_{r1} compensates the stray inductances. If the switching frequency is selected equal to (or slightly below, to facilitate load-independent soft-switching for the primary-side MOSFETs using the transformer magnetizing current) the resonant frequency, so-called "DC transformer" (DCX) behavior results [14], [15] as explained in **Fig. 7**. Advantageously, the DCX couples the output voltage tightly to the input voltage without the need for closed-loop control. Therefore, there is no need for a communication link between the primary and the secondary side, and black-start capability is easily achieved. Thus, the DCX concept has been used since the 1990s for similar sliding transformer applications [4]. The series resistances (i.e., here mainly the primary-side winding resistance) lead to a load-dependent voltage reduction at the output, which, for high-efficiency systems, remains limited to a few volts, i.e., is uncritical for the considered application. Note that if a tightly regulated output voltage was required, a downstream DC-DC converter could be employed or quantum operation of the DCX [16] could be employed.

B. Operation with Multiple Receivers

Many linear drive systems require more than one mover per axis, i.e., multiple independent drives and power supplies. For
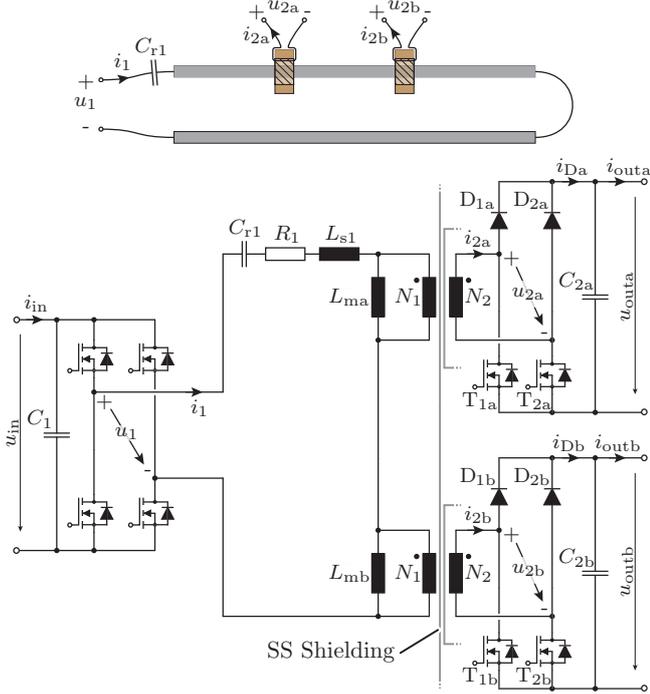
Fig. 8: PFC WPT with two receivers, conceptual physical arrangement and electrical equivalent circuit with power electronics necessary for its operation according to **Fig. 9**.

Fig. 9: Operation of a voltage-impressed DCX-based WPT system with two receivers using a time-sharing approach and mutually exclusive power transfer. Over a time-sharing period of $50T_{sw}$ (i.e., 50 switching cycles with $T_{sw} = 50\,\mu s$), each receiver consumes power during a relative on-time according to its load, see (5). This ensures equal average output voltages ($u_{outa} = u_{outb} \approx 67\,V$) for the considered unequal (resistive) loads $p_{outa} = 226.5\,W$ and $p_{outb} = 150\,W$.

example, **Fig. 8** shows a PFC WPT system with two receivers ('a' and 'b') and its equivalent circuit.

Various options for realizing WPT systems with multiple receivers have been discussed in literature. The most common and straightforward approach impresses a fixed primary current i_1 (see, e.g., [17], [18]), which allows each receiver to independently control its power intake (and ultimately the output voltage) by temporarily short-circuiting its secondary-side transformer winding (see, e.g., [19]–[21]). Since the magnetization inductances of the secondaries (e.g., L_{ma} and L_{mb} in **Fig. 8**) are connected in series, the primary-side current source must handle a high voltage if the receivers simultaneously take power and a low voltage when none of the receivers takes power. This and the impressed circulating current ultimately leads to low efficiency, especially in linear motion systems with relatively long primary windings.

Therefore, we employ an alternative approach that retains the voltage-impressed DCX operation and achieves output voltage control for multiple secondaries by supplying them with power on a cyclic basis in a mutually exclusive fashion, i.e., only one receiver is connected to the link at any given time. For example, when the receiver 'a' is powered, the switches $T_{\{1,2\}a}$ are open and the switches $T_{\{1,2\}b}$ are closed such that the receiver 'b' does not take any power.

To control the output voltages, each receiver can consume power during multiple switching periods before handing over to the next receiver. The relative on-times depend on the

respective output powers as

$$D_i = \frac{P_i}{\sum_k P_k}, \text{ i.e., } D_a = \frac{P_a}{P_a + P_b} \text{ and } D_b = \frac{P_b}{P_a + P_b}, \quad (5)$$

under the simplifying assumption of equal (controlled) output voltages, i.e., $u_{outa} \approx u_{outb}$. It is expected that in this way the minimum possible primary rms current stress can be achieved for arbitrary power consumption of the receivers. **Fig. 9** shows exemplary simulation results for a fixed time-sharing period of $50T_{sw}$. Alternatively, a variable duration of the time-sharing period could be achieved with a link arbitration mechanism similar to Carrier Sense Multiple Access (CSMA) known from telecommunication systems, which would not need a dedicated communication channel between the receivers and the primary. This control concept will be described in a future publication.

IV. Design Space and Measurement Results

Based on the specifications (i.e., dimensions from **Fig. 3**, input/output voltages of 72 V DC, a power transfer of ideally more than 100 W), and using the modeling approach and operating mode described in the preceding sections, we

(a)

(b)

(c)
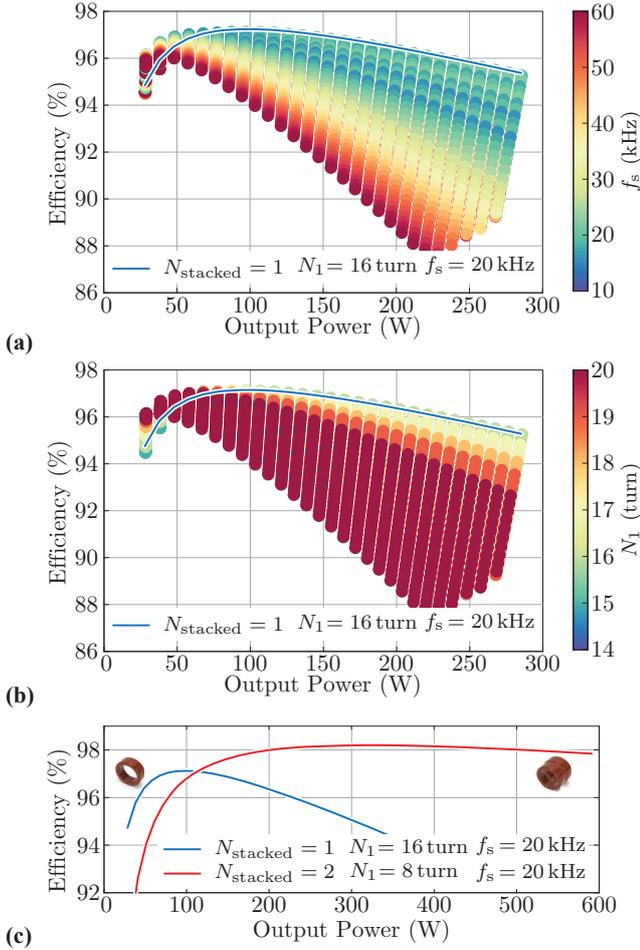
Fig. 10: Efficiency versus output power in dependence of **(a)** the operating frequency f_s and **(b)** the number of turns in the primary N_1 (note that $N_1 = N_2$ is used because of equal input and output DC voltages). The blue line indicates the best design with one stacked core ($N_\text{stacked} = 1$, $N_1 = 16$ turn, $f_s = 20$ kHz). **(c)** Higher efficiency and/or power transfer can be achieved with two cores ($N_\text{stacked} = 2$), which allows to halve the number of turns N_1 for the same magnetic flux density amplitude (i.e., pairs of conductors of the initial winding configuration are connected in parallel), resulting in lower winding resistance R_1.

then optimize the remaining degrees of freedom (number of turns, operating frequency, core cross section) for a single-secondary demonstrator. **Fig. 10** gives an overview on the results. These consider three different toroidal Vitroperm 500F core geometries (R50/40/20, R52/40/25 and R55/40/25) that provide sufficient inner diameter to match the given SS tube ($d_\text{ss} = 20$ mm). Furthermore, a single flat wire thickness ($\delta_\text{w} = 0.9$ mm) has been considered (the width depends on the number of turns N_1 as $w_\text{w} = d_w \pi / N_1 - b_\text{w}$).

Fig. 10(c) indicates how the initial design (blue line) can be modified to suit applications with higher power demand: by stacking two cores (i.e., doubling the core cross-sectional area), the number of primary turns can be halved (advantageously, from a variant point of view, by externally paralleling pairs of the original turns and hence with the identical primary

(a)

(b)
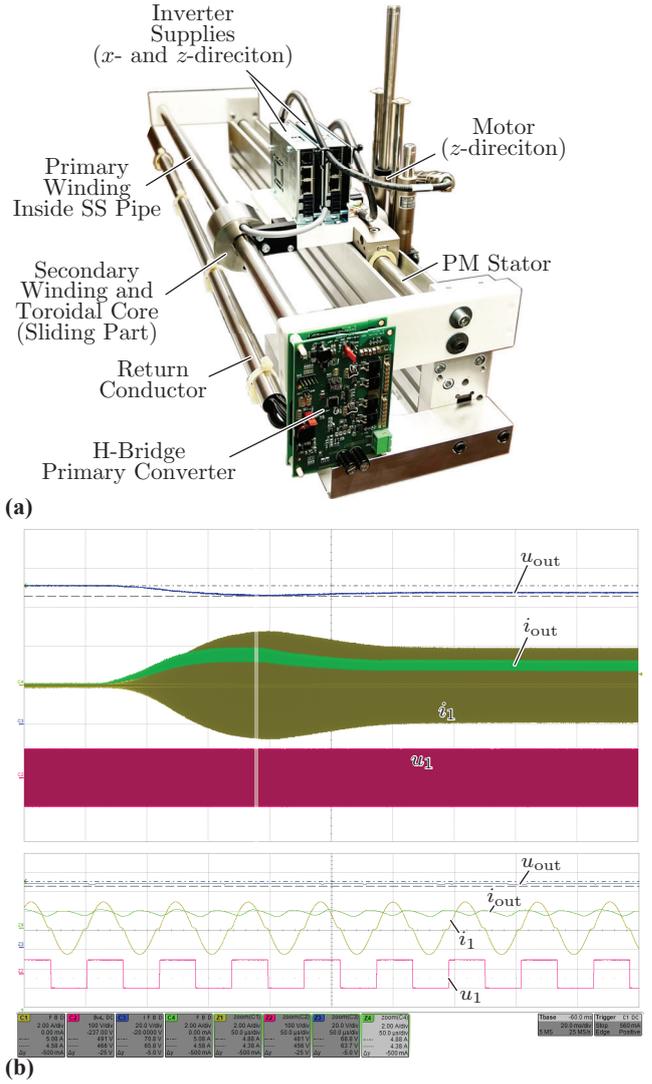
Fig. 11: (a) First industrial prototype of a linear x-z actuator with a PFC WPT system. Note that the relevant parts (i.e., the primary winding as well as the secondary-side core/winding assembly) are already fully enclosed in 0.5 mm SS. The inverters supplying the linear motors are attached to move together with the linear actuator's slider (in the x-direction). **(b)** Measured key waveforms during a mechanical load step applied to the z-direction linear motor. The output current i_out increases according to the power demand of the linear motor drive, and, with certain dynamics as expected from **Fig. 7(d)**, the transformer current amplitude i_1 increases and adjusts to the new operating point. The observed (minor) reduction of the output voltage is a consequence of the total series resistance.

winding / SS tube assembly), reducing the winding resistance R_1 accordingly.

A first industrial prototype is realized and the high-efficiency (up to 97%) WPT through SS is verified with measurements. The prototype is shown in **Fig. 11(a)**. The measurement results verifying power transfer to the linear motor during a mechanical load step are depicted in **Fig. 11(b)** and confirm the expected behavior of the DCX system, i.e., good load regulation without the need for a closed-loop control system.

V. CONCLUSIONS

In this paper, a concept for high-efficiency (97 % at 100 W) wireless power transfer (WPT) through stainless-steel (SS) enclosures is proposed to supply linear actuators for high-purity environments such as in pharmaceutical and food-processing industries. The magnetic field needed for WPT is oriented in parallel with the SS enclosure sheets to minimize the eddy-current losses, which is achieved with a coaxial arrangement of the WPT system. We provide a detailed analysis and modeling of the resulting residual losses in the SS enclosures and in the primary windings, which yields insights into the design trade-offs and optimum arrangements. We operate the WPT system as a series-resonant "DC transformer" (DCX), which facilitates good load regulation without the need for closed-loop control in case of a single receiver. Furthermore, a concept extending the system to multiple receivers is briefly discussed. Finally, the experimental results of a full industrial hardware demonstrator, i.e., a two-axis linear actuator supplied with WPT through SS, confirm the presented analysis.

REFERENCES

[1] B. L. Gysen, T. P. van der Sande, J. J. Paulides, and E. A. Lomonova, "Efficiency of a regenerative direct-drive electromagnetic active suspension," *IEEE Trans. Veh. Technol.*, vol. 60, no. 4, pp. 1384–1393, 2011.

[2] S. Mirić, P. Küttel, A. Tüysüz, and J. W. Kolar, "Design and experimental analysis of a new magnetically levitated tubular linear actuator," *IEEE Trans. Ind. Electron.*, vol. 66, no. 6, pp. 4816–4825, 2018.

[3] K. W. Klontz, D. M. Divan, D. W. Novotny, and R. D. Lorenz, "Contactless power delivery system for mining applications," *IEEE Trans. Ind. Appl.*, vol. 31, no. 1, pp. 27–35, 1995.

[4] J. M. Barnard, J. A. Ferreira, and J. D. van Wyk, "Sliding transformers for linear contactless power delivery," *IEEE Trans. Ind. Electron.*, vol. 44, no. 6, pp. 774–779, 1997.

[5] S. Hasanzadeh and S. Vaez-Zadeh, "Design of a wireless power transfer system for high power moving applications," *Progress in Electromagnetics Research M*, vol. 28, pp. 258–271, 2013.

[6] G. A. Covic and J. T. Boys, "Inductive power transfer," *Proc. IEEE*, vol. 101, no. 6, pp. 1276–1289, 2013.

[7] K. Moriki, A. Kawamura, T. Shimono, T. Nozaki, K. Ikeda, J. Sato, H. Hayashiya, and H. Yamamoto, "Technological feasibility of coaxial contactless power transmission for traction power supply," in *Proc. 16th IEEE Int. Power Electron. Motion Control Conf. Expo. (EPE-PEMC)*, Antalya, Turkey, Sep. 2014, pp. 967–972.

[8] S. Mirić, M. Tatić, J. Huber, D. Bortis, and J. W. Kolar, ""Pushing power through walls" – Wireless power transfer through stainless steel," in *Proc. 24th IEEE Int. Conf. Electr. Machines Syst. (ICEMS)*, Gyeongju, Korea, Oct. 2021, pp. 743–751.

[9] H. Ishida, T. Kyoden, and H. Furukawa, "Super-low frequency wireless power transfer with lightweight coils for passing through a stainless steel plate," *Rev. Sci. Instrum.*, vol. 89, no. 3, 2018.

[10] K. Küpfmüller, *Einführung in die theoretische Elektrotechnik (in German)*. Springer-Verlag, 2013.

[11] R. Garcia, A. Escobar-Mejia, K. George, and J. C. Balda, "Loss comparison of selected core magnetic materials operating at medium and high frequencies and different excitation voltages," in *Proc. IEEE Int. Symp. Power Electron. Distributed Generation Syst. (PEDG)*, Galway, Ireland, Aug. 2014.

[12] A. Esser and H.-C. Skudelny, "A new approach to power supplies for robots," *IEEE Trans. Ind. Appl.*, vol. 27, no. 5, pp. 872–875, 1991.

[13] J. E. Huber, J. Miniböck, and J. W. Kolar, "Generic derivation of dynamic model for half-cycle DCM series resonant converters," *IEEE Trans. Power Electron.*, vol. 33, no. 1, pp. 4–7, 2017.

[14] F. C. Schwarz, "A method of resonant current pulse modulation for power converters," *IEEE T. Ind. El. Con. In.*, vol. IECI-17, no. 3, pp. 209–221, May 1970.

[15] W. McMurray, "The thyristor electronic transformer: A power converter using a high-frequency link," *IEEE Trans. Ind. Gen. A.*, vol. IGA-7, no. 4, pp. 451–457, Jul. 1971.

[16] G. B. Joung, C. Rim, and G.-H. Cho, "Modeling of quantum series resonant converters - controlled by integral cycle mode," in *Conf. Rec. IEEE Ind. Appl. Soc. Annu. Meet.*, Pittsburgh, PA, USA, Oct. 1988, pp. 821–826.

[17] A. Kelley and W. Owens, "Connectorless power supply for an aircraft-passenger entertainment system," *IEEE Trans. Power Electron.*, vol. 4, no. 3, pp. 348–354, Jul. 1989.

[18] A. W. Green and J. T. Boys, "10 kHz inductively coupled power transfer - Concept and control," in *Proc. 5th Int. Conf. Power Electron. Variable-Speed Drives*, London, UK, Jan. 1994, pp. 694–699.

[19] F. F. Van der Pijl, P. Bauer, J. A. Ferreira, and H. Polinder, "Quantum control for an experimental contactless energy transfer system for multiple users," in *Proc. IEEE Power Electron. Spec. Conf. (PESC)*, Orlando, FL, USA, Oct. 2007, pp. 343–349.

[20] A. Welleman, S. Gekenidis, and R. Leutwyler, "A medium voltage fully controllable solid state switch for Klystrom modulator," in *Proc. IEEE Int. Power Modulator High Voltage Conf. (IPMHVC)*, Atlanta, GA, USA, May 2010, pp. 174–177.

[21] J. Gottschlich, M. Schäfer, M. Neubert, and R. W. De Doncker, "A galvanically isolated gate driver with low coupling capacitance for medium voltage SiC MOSFETs," in *Proc. 18th Europ. Conf. Power Electron. Appl. (EPE/ECCE Europe)*, Karlsruhe, Germany, Sep. 2016.